TECHNISCHE MECHANIK
European Journal of Engineering Mechanics
Diamond Open Access
journal homepage: www.ovgu.de/techmech

Tech. Mech., Vol. 46, Is. 1, (2026), 115–125
Received: 02.11.2025
Accepted: 08.01.2026
Available online: 16.02.2026

Analysis of externally excited nonlinear Mathieu equation model for floating bodies

Erik Silva Fujiyama[1], Josh Davidson[2], Tamás Kalmár-Nagy[1⋆]

[1] Budapest University of Technology and Economics, Department of Fluid Mechanics, Bertalan Lajos u. 4-6., 1111 Budapest, Hungary
[2] Basque Center for Applied Mathematics, Mazarredo 14, 48009 Bilbao, Spain

Abstract: Parametric resonance is a dynamic instability that causes exponential growth in the amplitude of an oscillating system. This study performs a nondimensional analysis on a nonlinear Mathieu-type equation model for floating bodies excited by waves, developed to capture parametric resonance in both the heave and pitch degrees of freedom. A non-cylindrical axisymmetric spar-buoy is used as a test case. The wave excitation forces are pre-calculated for various heave and pitch positions and interpolated with a third-order polynomial. The model includes nonlinear hydrostatic restoring forces and incorporates position-dependency of the wave excitation forces. Through the nondimensional analysis, the model is simplified. Simulations show parametric resonance when the wave frequency is twice the natural frequency of the structure. The behaviour of the oscillations is investigated by a frequency sweep. The results compare favourably to those from a benchmark model with nonlinear Froude-Krylov forces, but achieving a 10000-fold speed increase, with the computation time going from at least three hours, to less than one second. On top of this increased computational efficiency, the presented model facilitates analytical approaches, such as perturbation analysis or harmonic balance.

Keywords: Mathieu equation, nonlinear hydrodynamic modelling, parametric resonance, spar-buoy

1 Introduction

Parametric resonance is a dynamic instability that causes exponential growth in the amplitude of an oscillating system. For example, it occurs in differential equations with time-varying coefficients Nayfeh and Mook (2008). The most well-known example of such equations is the Mathieu equation, a second-order ordinary differential equation (ODE) with no external forcing and a harmonically time-varying parameter.
Various phenomena, such as the oscillation of floating bodies, are described by the Mathieu equation and its variants, as in Koo et al. (2004); Aziminia et al. (2022). The time-varying parameter normally represents a part of the hydrostatic stiffness and leads to heave-to-pitch instability.
Heave-to-heave instabilities, on the other hand, caused by a non-constant cross-sectional area in the body, are rarely found in the literature. This type of instability was studied numerically in Jang and Kim (2019) for the case of an Arctic Spar. In Lelkes et al. (2021), an analytical model was developed to capture the heave-to-heave parametric instability. In Lelkes et al. (2021), the occurrence of parametric resonance in the heave was not induced by the nonlinear hydrostatic stiffness term, but rather by the dependency of the wave excitation force on the heave position. This dependency was obtained through the interpolation of the wave excitation force calculated at various positions. Rodríguez and Neves (2012) also consider positional dependence of hydrodynamic forces, applying a different approach in which a Taylor series expansion is applied to a simplified approximation of the force near equilibrium. In Fujiyama et al. (2025), the model developed in Lelkes et al. (2021) was expanded to also include the pitch. In this paper, we evaluate the significance of the parameters in the model presented in Fujiyama et al. (2025) by nondimensionalization, and thus reduce the number of nonlinear terms in the interpolation, making the model simpler and faster. We also investigate the bifurcation structure of the model using a forward and backward frequency sweep and square-root type of fit to the response amplitudes. The NLFK force model Giorgi et al. (2021) is used as the benchmark.

2 The parametric excitation model

In this section, we present the model from Lelkes et al. (2021), extended to two degrees of freedom (DoF) in Fujiyama et al. (2025), to describe the motion of a spar-buoy under harmonic wave excitation.
In Fig. 1, a floating body is shown along with the world coordinate system $\boldsymbol{ij}$. The origin of this system is horizontally aligned with the body's center of gravity (cog) and vertically at the still water level (SWL), which represents the water surface elevation without the waves. The motion of the body is constrained to the heave DoF z, i.e. vertical motion in the $\boldsymbol{j}$ axis, and the pitch DoF φ, i.e. rotation around the center of gravity. The wave elevation η is measured relative to the SWL. By convention, the wave propagation direction follows the direction of the $\boldsymbol{i}$ axis.
Only harmonic wave elevations, defined as

$$\eta(t) = \frac{H}{2} \cdot \cos(\omega t), \tag{1}$$

⋆ E-mail address: kalmar.nagy.tamas@gpk.bme.hu
doi: 10.24352/UB.OVGU-2026-012

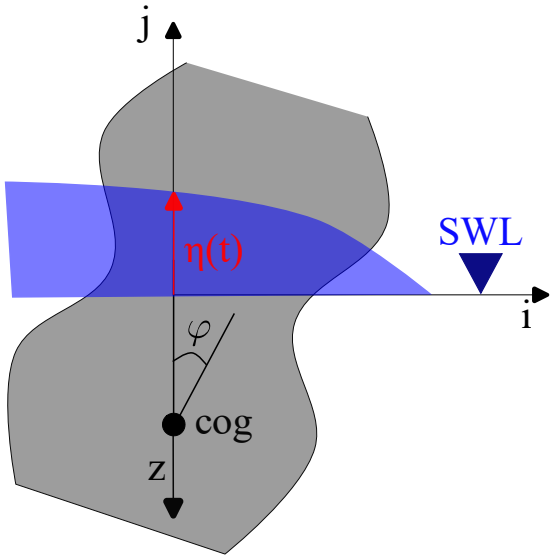

Fig. 1: Floating body, wave elevation, and the world coordinate system for two DoFs

where H is the wave height and ω is the wave frequency, are considered.
The 2-DoF model presented in Fujiyama et al. (2025) is

$$\left(m_{\text{body}} + m_{\text{a}}\left(\omega\right)\right)\ddot{z} + m_{\text{a2}}\ddot{\varphi} + c_{\text{a}}\dot{z} + c_{\text{a3}}\dot{\varphi} + F_{\text{hr}}(z,\varphi) = F_{\text{e}}(z,\varphi,t,\omega,H), \tag{2}$$

$$\left(I + I_{\text{a}}\right)\ddot{\varphi} + I_{\text{a2}}\ddot{z} + c_{\text{a2}}\dot{\varphi} + c_{\text{a4}}\dot{z} + M_{\text{hr}}(z,\varphi) = M_{\text{e}}(z,\varphi,t,\omega,H), \tag{3}$$

where m_{body} is the mass of the floating body, $m_{\text{a}}\left(\omega\right)$ and m_{a2} are the added masses, c_{a}, c_{a2}, c_{a3}, and c_{a4} are the radiation damping coefficients, F_{hr} is the hydrostatic restoring force, F_{e} is the wave excitation force, I is the rotational inertia, I_{a} and I_{a2} are the added rotational inertia, M_{hr} is the hydrostatic restoring moment, and M_{e} is the wave excitation moment.

3 The test case and its modeling

3.1 The test case

The test case considered is the same one used in Lelkes et al. (2021) and in Fujiyama et al. (2025). The test case is an axisymmetric spar-buoy with the cross-section shown in Fig. 2.
The conic shape of the buoy is defined by

$$f_{\text{buoy}}(\varsigma) = \begin{cases} \Gamma_1 & -\left(\frac{h_0}{2} + h_1\right) \leq \varsigma < -\frac{h_0}{2}, \\ \Gamma_0 + \varsigma\tan(\alpha) & -\frac{h_0}{2} \leq \varsigma \leq \frac{h_0}{2}, \\ 0 & \text{otherwise.} \end{cases} \tag{4}$$

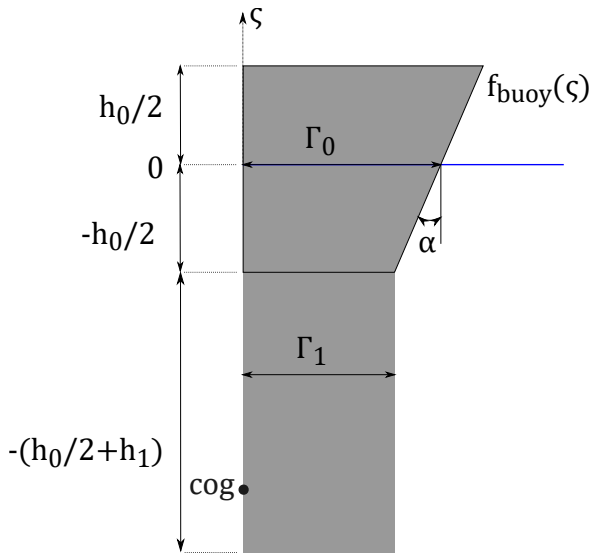

Fig. 2: Section of the spar-buoy geometry

The physical parameters of the spar-buoy and their corresponding values are listed in Tab. 1. The water density is set to $\rho_{\text{water}} = 1025$ kg/m^3 and the gravitational acceleration to $g = 9.806$ m/s^2.
Even though the mass m_{body} is in Tab. 1, it is a derived quantity from the geometrical parameters of the system at equilibrium. At $z = 0$, the buoyancy force is at equilibrium with the weight, so the mass m_{body} must be

$$m_{\text{body}} = V(0,0)\rho, \tag{5}$$

where $V(0,0)$ is the submerged volume at the equilibrium position.

3.2 Modeling of the test case

The hydrostatic restoring terms F_{hr} and M_{hr} are calculated based on the body geometry with

$$F_{\text{hr}}(z,\varphi) = \rho_{\text{water}} g \Delta V(z,\varphi), \tag{6}$$

where $\Delta V(z,\varphi) = V(z,\varphi) - V(0,0)$, $V(z,\varphi)$ being the submerged volume, and

$$M_{\text{hr}}(z,\varphi) = \rho g \Delta V(z,\varphi) \cdot (x_{\text{cob}}(z,\varphi) - x_{\text{cog}}), \tag{7}$$

where $x_{\text{cob}}(z,\varphi)$ is the horizontal position of the center of buoyancy, and x_{cog} is the horizontal position of the center of gravity.
In this case $F_{\text{hr}}(z,\varphi)$ and $M_{\text{hr}}(z,\varphi)$ are calculated numerically with the CAD software FreeCAD Machado et al. (2019). The values for $F_{\text{hr}}(z,\varphi)$ and $M_{\text{hr}}(z,\varphi)$ are determined for a set of discrete pitch angles ranging from -0.21 rad to 0.21 rad, with a step size of 0.07 rad, and for heave displacements from -4 m to 4 m, with a step size of 1 m.
An interpolation is then performed on the generated dataset to continuously represent $F_{\text{hr}}(z,\varphi)$ and $M_{\text{hr}}(z,\varphi)$, employing polynomial functions of the heave z and pitch φ displacement. The resulting polynomial expressions are

$$F_{\text{hr}}(z,\varphi) = \rho g \Delta V(z,\varphi) \approx \sum_{1 \le \text{i+j} \le 3} r_{\text{i,j}} z^{\text{i}} \varphi^{\text{j}}, \tag{8}$$

$$M_{\text{hr}}(z,\varphi) = \rho g \Delta V(z,\varphi)(x_{\text{cob}}(z,\varphi) - x_{\text{cog}}) \approx \sum_{1 \le \text{i+j} \le 3} s_{\text{i,j}} z^{\text{i}} \varphi^{\text{j}}, \tag{9}$$

where $r_{\text{i,j}}$ are the hydrostatic restoring coefficients for the heave obtained from the polynomial interpolation, $s_{\text{i,j}}$ are the hydrostatic restoring coefficients for the pitch obtained from the polynomial interpolation.
The wave excitation terms are divided into two components, the Froude-Krylov terms F_{FK} and M_{FK}, as well as the diffraction terms F_{diff} and M_{diff} as

$$F_{\text{e}}(z,\varphi,t,\omega,H) = F_{FK}(z,\varphi,t,\omega,H) + F_{\text{diff}}(t,\omega,H), \tag{10}$$

$$M_{\text{e}}(z,\varphi,t,\omega,H) = M_{FK}(z,\varphi,t,\omega,H) + M_{\text{diff}}(t,\omega,H), \tag{11}$$

where

$$\begin{aligned}
F_{FK}(z,\varphi,t,\omega,H) &= \frac{H}{2} f_{FK}(z,\varphi,\omega)\cos(\omega t - \theta_{FK}(z,\varphi,\omega)),\\
M_{FK}(z,\varphi,t,\omega,H) &= \frac{H}{2} m_{FK}(z,\varphi,\omega)\cos(\omega t - \theta_{FK2}(z,\varphi,\omega)),\\
F_{\text{diff}}(t,\omega,H) &= \frac{H}{2} f_{\text{diff}}(\omega)\cos(\omega t - \theta_{\text{diff}}(\omega)),\\
M_{\text{diff}}(t,\omega,H) &= \frac{H}{2} m_{\text{diff}}(\omega)\cos(\omega t - \theta_{\text{diff2}}(\omega)).
\end{aligned} \tag{12}$$

Here, the diffraction terms are considered independent of the buoy's position, since the diffraction force is commonly considered small and linear Giorgi et al. (2021), or even negligible Folley (2016).

Tab. 1: Physical parameters of the spar-buoy

Parameter	Symbol	Value	Units
Angle of the conical part	α	0.197	rad
Radius of the conical part at equilibrium state at still water level	Γ_0	3	m
Length of the conical part	h_0	10	m
Length of the cylindrical extension	h_1	15	m
Radius of the cylindrical extension	Γ_1	2	m
Mass	m_{body}	$2.95 \cdot 10^5$	kg
Vertical position of center of gravity	z_{cog}	-16	m
Moment of inertia	I	$1.18 \cdot 10^7$	kg·m^2

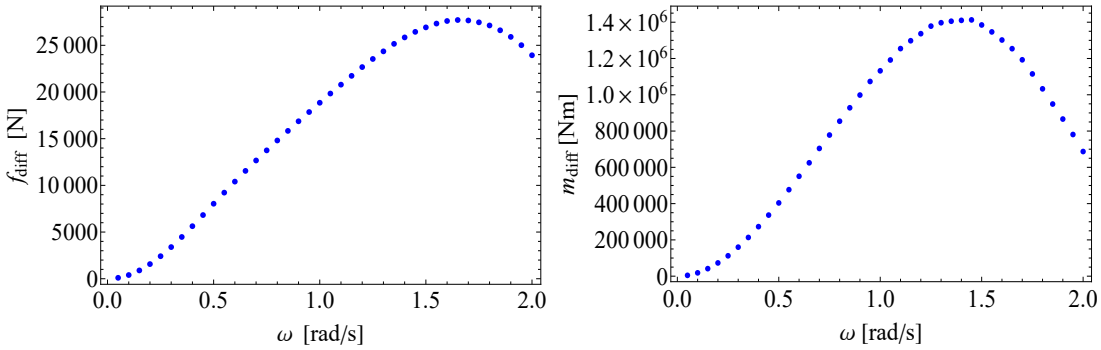

(a) $f_{\text{diff}}(\omega)$ (b) $m_{\text{diff}}(\omega)$

Fig. 3: Diffraction amplitude coefficients calculated with NEMOH

The amplitude coefficients $f_{FK}(z,\varphi,\omega)$, $m_{FK}(z,\varphi,\omega)$, $f_{\text{diff}}(\omega)$, $m_{\text{diff}}(\omega)$, and the phase coefficients $\theta_{FK}(z,\varphi,\omega)$, $\theta_{FK2}(z,\varphi,\omega)$, $\theta_{\text{diff}}(\omega)$, $\theta_{\text{diff2}}(\omega)$ are obtained using the open-source boundary element solver NEMOH Babarit and Delhommeau (2015); Kurnia and Ducrozet (2023, 2022), which computes first-order hydrodynamic coefficients, such as added mass, radiation and excitation forces in the frequency domain. NEMOH employs linear potential flow theory for an inviscid, incompressible, irrotational fluid. By assuming small motions around the mean position and using linearized free surface equations Folley (2016), NEMOH solves the boundary value problem to obtain all the hydrodynamic coefficients. Here, the settings for the mesh are 400 angular segments and 500 panels.

A significant limitation of the linear potential flow method is the assumption of small motions, which restrains the accuracy of the calculations to small displacements around the equilibrium position of a floating body. To address this limitation, the parametric excitation model employs a multi-linear approach, computing the excitation force coefficients at various positions of the floating body and then interpolating these values with polynomials. The excitation force is then computed by multiplying the free surface elevation by the position-dependent interpolated excitation force coefficients potentially providing a more accurate simulation of larger motions.

Here, the Froude-Krylov coefficients are computed for the same discrete displacements used in the hydrostatic restoring terms. The Froude-Krylov terms are also interpolated with polynomial functions, yielding the following expressions

$$F_{FK}(t,\omega,z,\varphi,H) \approx \frac{H}{2}\cos\left(\omega t - \sum_{0\le i+j\le 1} d_{i,j}(\omega) z^i \varphi^j\right) \sum_{0\le i+j\le 3} a_{i,j}(\omega) z^i \varphi^j, \tag{13}$$

$$M_{FK}(t,\omega,z,\varphi,H) \approx \frac{H}{2}\cos\left(\omega t - \sum_{0\le i+j\le 2} f_{i,j}(\omega) z^i \varphi^j(\omega)\right) \sum_{0\le i+j\le 3} b_{i,j}(\omega) z^i \varphi^j, \tag{14}$$

where $d_{i,j}$, $a_{i,j}$, $f_{i,j}$ and $b_{i,j}$ are the coefficients obtained from the polynomial interpolation. The frequency dependency of the wave excitation coefficients is shown in the figures of Appendix B of Fujiyama et al. (2025), where they were obtained using the complete third-order polynomial interpolation.

The total excitation force and moment therefore expressed as

$$F_e(t,\omega,z,\varphi,H) \approx \frac{H}{2} f_{\text{diff}}(\omega)\cos(\omega t - \theta_{\text{diff}}(\omega)) + \frac{H}{2}\cos\left(\omega t - \sum_{0\le i+j\le 1} d_{i,j}(\omega) z^i \varphi^j\right) \sum_{0\le i+j\le 3} a_{i,j}(\omega) z^i \varphi^j, \tag{15}$$

$$M_e(t,\omega,z,\varphi,H) \approx \frac{H}{2} m_{\text{diff}}(\omega)\cos(\omega t - \theta_{\text{diff2}}(\omega)) + \frac{H}{2}\cos\left(\omega t - \sum_{0\le i+j\le 2} f_{i,j}(\omega) z^i \varphi^j(\omega)\right) \sum_{0\le i+j\le 3} b_{i,j}(\omega) z^i \varphi^j, \tag{16}$$

The diffraction coefficients are shown in Fig. 3 and 4.

The radiation and added mass coefficients m_a, m_{a2}, I_a, I_{a2}, c_a, c_{a2}, c_{a3} and c_{a4} in Eqs. (2) and (3) are also computed using NEMOH. The cross terms m_{a2}, c_{a3}, I_{a2} and c_{a4} were over four orders of magnitude smaller than the other coefficients. This outcome is expected for an axisymmetric body, and these coefficients were subsequently neglected.

In general, a body oscillates at the same frequency as the non-resonant excitation. When parametric excitation occurs the body oscillates at half of the wave frequency. Here we follow Lelkes et al. in Lelkes et al. (2021), the radiation damping considered is the function of the wave excitation frequency, not that of the motion of the body. This approach has the following limitation. Where parametric resonance occurs, the body oscillates at half of the wave frequency. Thus we are evaluating forces corresponding to the wrong oscillation frequency. The wave excitation forces, which are the primary focus of the model, are not significantly affected. Simplifications of this kind are not uncommon in literature, as seen in works such as Davidson and Kalmár-Nagy (2020); Gavassoni et al. (2014); Hong et al. (2005), where the radiation damping was similarly treated to focus on other specific aspects of the analysis. The radiation coefficients with their frequency dependency are shown in Fig. 5.

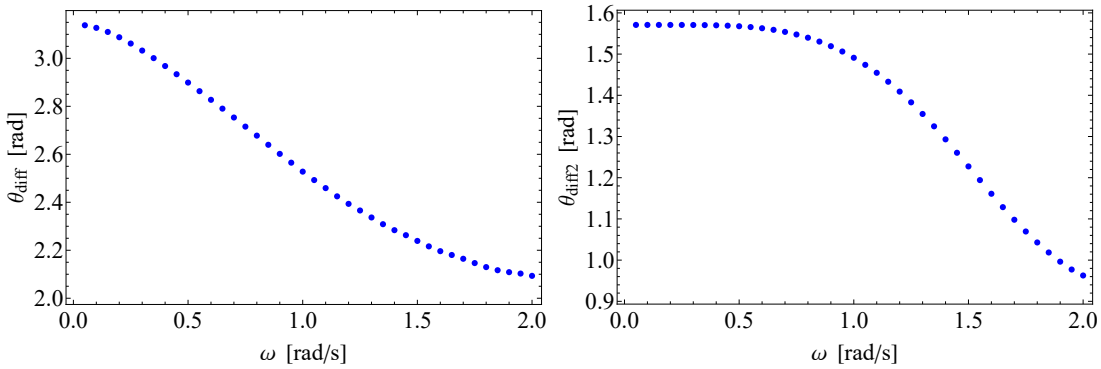

(a) $\theta_{\text{diff}}(\omega)$ (b) $\theta_{\text{diff2}}(\omega)$

Fig. 4: Diffraction phase coefficients calculated with NEMOH

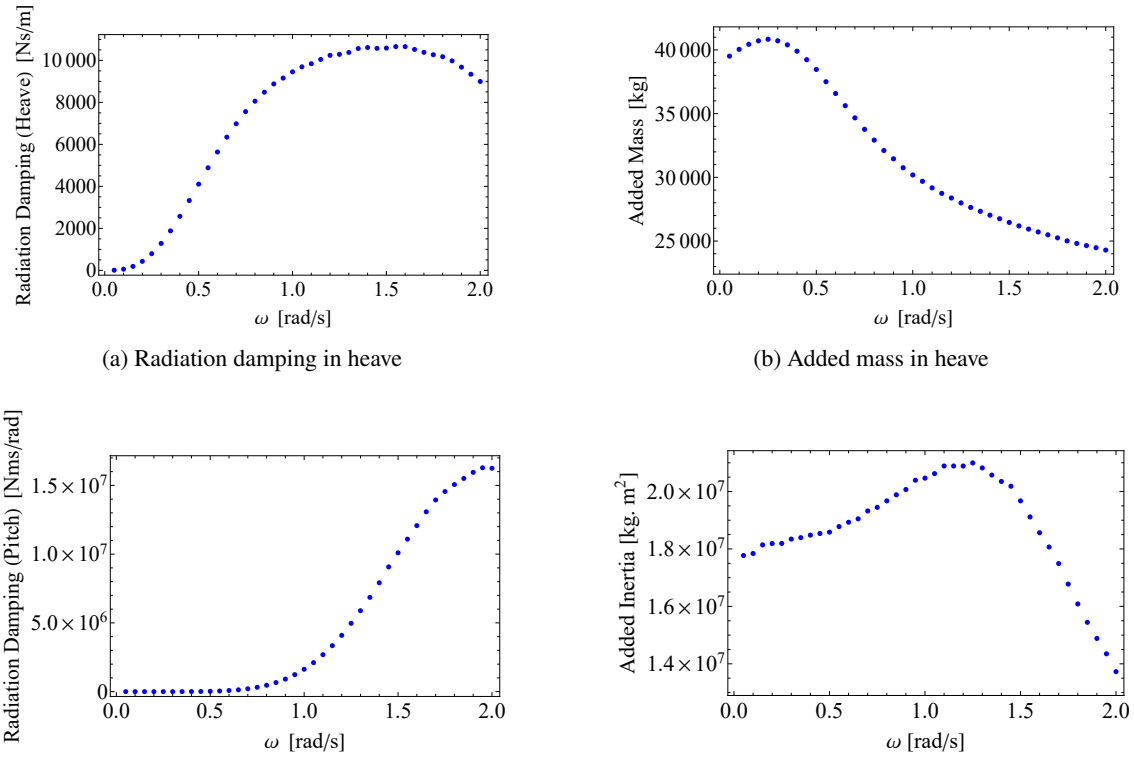

(a) Radiation damping in heave (b) Added mass in heave

(c) Radiation damping in pitch (d) Added inertia in pitch

Fig. 5: Hydrodynamic coefficients of radiation forces and moments calculated by NEMOH

The equations for the parametric excitation model then become

$$(m_{\text{body}} + m_{\text{a}}(\omega))\ddot{z} + c_{\text{a}}(\omega)\dot{z} + \sum_{1\le \text{i+j}\le 3} r_{\text{i,j}} z^{\text{i}}\varphi^{\text{j}} = \frac{H}{2} f_{\text{diff}}(\omega)\cos(\omega t - \theta_{\text{diff}}(\omega)) + \frac{H}{2}\cos\left(\omega t - \sum_{0\le \text{i+j}\le 1} d_{\text{i,j}}(\omega) z^{\text{i}}\varphi^{\text{j}}\right) \sum_{0\le \text{i+j}\le 3} a_{\text{i,j}}(\omega) z^{\text{i}}\varphi^{\text{j}}, \tag{17}$$

$$(I + I_{\text{a}}(\omega))\ddot{\varphi} + c_{\text{a2}}(\omega)\dot{\varphi} + \sum_{1\le \text{i+j}\le 3} s_{\text{i,j}} z^{\text{i}}\varphi^{\text{j}} = \frac{H}{2} m_{\text{diff}}(\omega)\cos(\omega t - \theta_{\text{diff2}}(\omega)) + \frac{H}{2}\cos\left(\omega t - \sum_{0\le \text{i+j}\le 2} f_{\text{i,j}}(\omega) z^{\text{i}}\varphi^{\text{j}}\right) \sum_{0\le \text{i+j}\le 3} b_{\text{i,j}}(\omega) z^{\text{i}}\varphi^{\text{j}}. \tag{18}$$

As the hydrostatic restoring and the excitation coefficients were calculated for

$$|z| \le 4 \text{ m}, |\varphi| \le 0.21 \text{ rad}, \tag{19}$$

this is referred to as the validity region of the model.

4 Nondimensionalization and simplification

In order to better understand the significance of the parameters in the parametric excitation model and remove terms that do not alter the results, Eqs. (17) and (18) are nondimensionalized. The nondimensional variables are defined as follows,

$$\tilde{t} = \frac{t}{T}, \tilde{z} = \frac{z}{Z}, \tilde{\varphi} = \frac{\varphi}{\Phi}. \tag{20}$$

As the validity region of the model is defined as $|z| \leq 4$ m and $|\varphi| \leq 0.21$ rad (as stated in Section 3), the scales Z and Φ are defined so that $\tilde{z}$ and $\tilde{\varphi}$ are between -1 and 1, i.e.

$$Z = 4 \text{ m}, \Phi = 0.21 \text{ rad}. \tag{21}$$

The time scale T is defined as

$$T = \sqrt{\frac{m_{\text{body}} + m_{\text{a}}(\omega)}{r_{1,0}}}. \tag{22}$$

The nondimensional equations become

$$\tilde{z}'' + \alpha_3(\omega)\tilde{z}' + \sum_{1\leq \text{i+j}\leq 3} \gamma_{\text{i,j}}(\omega)\tilde{z}^{\text{i}}\tilde{\varphi}^{\text{j}} = \cos\left(\nu\tilde{t} - \sum_{0\leq \text{i+j}\leq 1} \xi_{\text{i,j}}(\omega)\tilde{z}^{\text{i}}\tilde{\varphi}^{\text{j}}\right) \sum_{0\leq \text{i+j}\leq 3} \beta_{\text{i,j}}(\omega)\tilde{z}^{\text{i}}\tilde{\varphi}^{\text{j}} + \kappa(\omega)\cos(\nu t - \theta_{\text{diff}}(\omega)), \tag{23}$$

$$\tilde{\varphi}'' + \alpha_5(\omega)\tilde{\varphi}' + \sum_{1\leq \text{i+j}\leq 3} \zeta_{\text{i,j}}(\omega)\tilde{z}^{\text{i}}\tilde{\varphi}^{\text{j}} = \cos\left(\nu\tilde{t} - \sum_{0\leq \text{i+j}\leq 2} \chi_{\text{i,j}}(\omega)\tilde{z}^{\text{i}}\tilde{\varphi}^{\text{j}}\right) \sum_{0\leq \text{i+j}\leq 3} \mu_{\text{i,j}}(\omega)\tilde{z}^{\text{i}}\tilde{\varphi}^{\text{j}} + \psi(\omega)\cos(\nu t - \theta_{\text{diff2}}(\omega)), \tag{24}$$

where the derivatives with regards to the nondimensional time are denoted by $'$, and the nondimensional parameters are

$$\begin{aligned}
&\alpha_3(\omega) = \frac{c_{\text{a}}}{\sqrt{(m_{\text{body}} + m_{\text{a}}(\omega))r_{1,0}}}, \quad \alpha_5(\omega) = \frac{c_{\text{a2}}\sqrt{m_{\text{body}} + m_{\text{a}}(\omega)}}{(I + I_{\text{a}}(\omega))\sqrt{r_{1,0}}}, \quad \gamma_{\text{i,j}}(\omega) = \frac{1}{r_{1,0}} r_{\text{i,j}} Z^{i-1}\Phi^{\text{i}},\\
&\beta_{\text{i,j}}(\omega) = \frac{H}{r_{1,0}} a_{\text{i,j}} Z^{i-1}\Phi^{\text{i}}, \quad \zeta_{\text{i,j}}(\omega) = \frac{T^2}{I + I_{\text{a}}(\omega)} s_{\text{i,j}} Z^{\text{i}}\Phi^{i-1}, \quad \mu_{\text{i,j}}(\omega) = \frac{HT^2}{I + I_{\text{a}}(\omega)} b_{\text{i,j}} Z^{\text{i}}\Phi^{i-1},\\
&\nu(\omega) = \omega\sqrt{\frac{m_{\text{body}} + m_{\text{a}}(\omega)}{r_{1,0}}}, \quad \xi_{\text{i,j}}(\omega) = d_{\text{i,j}}(\omega) Z^{\text{i}}\Phi^{\text{j}}, \chi_{\text{i,j}}(\omega) = f_{\text{i,j}}(\omega) Z^{\text{i}}\Phi^{\text{j}}, \quad \kappa(\omega) = \frac{H}{2r_{1,0}} f_{\text{diff}}(\omega) Z^{-1},\\
&\psi(\omega) = \frac{HT^2}{2(I + I_{\text{a}}(\omega))} m_{\text{diff}}(\omega)\Phi^{-1}.
\end{aligned} \tag{25}$$

The restoring parameters are now functions of ω. To estimate their orders of magnitude, their values for $\omega = 1.9$ rad/s are calculated as

$$\alpha_3 = 0.03, \quad \alpha_5 = 0.63, \quad \nu = 2, \tag{26}$$

while to other quantities are collected in Tab. 2.

The nondimensional coefficients $\gamma_{\text{i,j}}$ and $\zeta_{\text{i,j}}$ correspond to the hydrostatic restoring coefficients $r_{\text{i,j}}$ and $s_{\text{i,j}}$. The coefficients $\beta_{\text{i,j}}$, $\mu_{\text{i,j}}$, $\xi_{\text{i,j}}$ and $\chi_{\text{i,j}}$ relate to the wave excitation coefficients $a_{\text{i,j}}$, $b_{\text{i,j}}$, $d_{\text{i,j}}$ and $f_{\text{i,j}}$, while α_3 and α_5 correspond to the radiation damping terms c_3 and c_5.

In Tab. 2, the nondimensional coefficients $\gamma_{0,1}$, $\gamma_{1,1}$, $\gamma_{2,1}$, $\zeta_{1,0}$, $\zeta_{2,0}$, $\zeta_{3,0}$, $\zeta_{0,2}$, and $\zeta_{1,2}$ have "small" values. This notion of smallness is based on our observation that the term $\gamma_{3,0}\tilde{z}^3$ was the term with the smallest coefficient whose exclusion affected the interpolation results by more than 1%.

Thus the polynomial interpolation for the hydrostatic restoring forces was carried out excluding terms corresponding to $\gamma_{0,1}$, $\gamma_{1,1}$, $\gamma_{2,1}$, $\zeta_{1,0}$, $\zeta_{2,0}$, $\zeta_{3,0}$, $\zeta_{0,2}$, and $\zeta_{1,2}$ (effectively forcing these coefficients to be 0).

By performing an interpolation for F_{hr} and M_{hr} without the coefficients corresponding to the small coefficients, the results shown in Tab. 3 were obtained.

The same procedure was applied to the wave excitation coefficients and led to the values in Tab. 4.

Our model is thus

$$\tilde{z}'' + \alpha_3(\omega)\tilde{z}' + F_{\text{ndhrsimplified}}(\tilde{z},\tilde{\varphi}) = \cos\left(\nu\tilde{t} - \theta_{\text{ndFKsimplified}}(\tilde{z},\tilde{\varphi},\omega)\right) f_{\text{ndFKsimplified}}(\tilde{z},\tilde{\varphi},\omega) + \kappa(\omega)\cos(\nu t - \theta_{\text{diff}}(\omega)), \tag{27}$$

$$\tilde{\varphi}'' + \alpha_5(\omega)\tilde{\varphi}' + M_{\text{ndhrsimplified}}(\tilde{z},\tilde{\varphi}) = \cos\left(\nu\tilde{t} - \theta_{\text{ndFK2simplified}}(\tilde{z},\tilde{\varphi},\omega)\right) m_{\text{ndFKsimplified}}(\tilde{z},\tilde{\varphi},\omega) + \psi(\omega)\cos(\nu t - \theta_{\text{diff2}}(\omega)), \tag{28}$$

where

$$
\begin{aligned}
F_{\text{ndhrsimplified}}(\tilde{z},\tilde{\varphi}) &= \gamma_{1,0}\tilde{z} + \gamma_{2,0}\tilde{z}^2 + \gamma_{3,0}\tilde{z}^3 + \gamma_{0,2}\tilde{\varphi}^2 + \gamma_{1,2}\tilde{z}\tilde{\varphi}^2,\\
M_{\text{ndhrsimplified}}(\tilde{z},\tilde{\varphi}) &= \zeta_{0,1}\tilde{\varphi} + \zeta_{0,3}\tilde{\varphi}^3 + \zeta_{1,1}\tilde{z}\tilde{\varphi} + \zeta_{2,1}\tilde{z}^2\tilde{\varphi},\\
f_{\text{ndFKsimplified}}(\tilde{z},\tilde{\varphi},\omega) &= \beta_{0,0}(\omega) + \beta_{1,0}(\omega)\tilde{z} + \beta_{2,0}(\omega)\tilde{z}^2 + \beta_{3,0}(\omega)\tilde{z}^3 + \beta_{0,2}(\omega)\tilde{\varphi}^2 + \beta_{1,2}(\omega)\tilde{z}\tilde{\varphi}^2,\\
m_{\text{ndFKsimplified}}(\tilde{z},\tilde{\varphi},\omega) &= \mu_{0,0}(\omega) + \mu_{1,0}(\omega)\tilde{z} + \mu_{2,0}(\omega)\tilde{z}^2 + \mu_{3,0}(\omega)\tilde{z}^3 + \mu_{0,2}(\omega)\tilde{\varphi}^2 + \mu_{1,2}(\omega)\tilde{z}\tilde{\varphi}^2,\\
\theta_{\text{ndFKsimplified}}(\tilde{z},\tilde{\varphi},\omega) &= \xi_{0,0}(\omega) + \xi_{0,1}(\omega)\tilde{\varphi},\\
\theta_{\text{ndFK2simplified}}(\tilde{z},\tilde{\varphi},\omega) &= \chi_{0,0}(\omega) + \chi_{0,1}(\omega)\tilde{\varphi} + \chi_{1,1}(\omega)\tilde{z}\tilde{\varphi}.
\end{aligned}
\tag{29}
$$

We refer to Eqs. (27) and (28) as the *simplified model*.

5 Results

The equations for the parametric excitation model (Eqs. (2) and (3)) and for the simplified model (Eqs. (27) and (28)) are solved numerically using the NDSolve function in Wolfram Mathematica 14.1 with its default settings: the LSODA method with adaptive timestep and a machine precision of 16 digits. The results are then converted back to dimensional values with Eqs. (20), (21) and (22), as they will be compared to the results of the NLFK force model (introduced later) that outputs dimensional values.
The natural frequencies for the heave DoF $\omega_{0\text{heave}} = 0.93$ rad/s and the pitch DoF $\omega_{0\text{pitch}} = 0.73$ rad/s are also found numerically by running a simulation without the external excitation. It is critical to note that the validity region of the simplified model is limited to the range over which the excitation and restoring force coefficients were computed, $|z| \leq 4$ m, and $|\varphi| \leq 0.21$ rad.
The difference at the steady-state between the parametric excitation model (Eqs. (2) and (3)) and the simplified model (Eqs. (27) and (28)) was negligible, as shown in Figs. 6 and 7.
A laptop was used with Intel(R) Core(TM) i7-8565U CPU @ 1.80GHz (1.99 GHz) and 16 GB of RAM. The interpolation required to obtain the coefficients for the parametric excitation model (Table 2) takes approximately 2 seconds, whereas the corresponding interpolation for the simplified model (Tables 3 and 4) requires about 0.3 second. In contrast, the time required to solve the equations is comparable for both models, differing by approximately 6%. Overall, the difference in computational time is modest. However, simplifying the polynomial expressions makes the model more amenable to analytical investigations. Such analysis may, in turn, enable the formulation of design optimization problems for key parameters, such as the spar-buoy radius and inclination angle, with the objective of maximizing or minimizing the resonance region and response amplitude.
The root mean square (rms) of the solutions $z(t)$ and $\varphi(t)$ were calculated with

$$
z_{\text{rms}} = \sqrt{\frac{1}{t_2 - t_1}\int_{t_1}^{t_2} z^2(t)\,dt}, \tag{30}
$$

$$
\varphi_{\text{rms}} = \sqrt{\frac{1}{t_2 - t_1}\int_{t_1}^{t_2} \varphi^2(t)\,dt}, \tag{31}
$$

with

$$
t_1 = 584 \cdot \frac{2\pi}{\omega},\ t_2 = 600 \cdot \frac{2\pi}{\omega}. \tag{32}
$$

Due to the presence of cubic nonlinearities in Eqs. (27) and (28), it is expected that the amplitudes of the oscillations would continue growing during a frequency sweep once parametric resonance is triggered as shown in Azimi (2022). In Fig. 8, a forward

Tab. 2: Nondimensional polynomial approximation coefficients for hydrostatic restoring terms ($\gamma_{\text{i,j}}$ and $\zeta_{\text{i,j}}$), and wave excitation terms ($\beta_{\text{i,j}}$, $\mu_{\text{i,j}}$, $\xi_{\text{i,j}}$, and $\chi_{\text{i,j}}$)

i,j	0, 0	1, 0	2, 0	3, 0	0, 1	0, 2	0, 3
$\gamma_{\text{i,j}}$	0	0.21	-0.012	$2.26 \cdot 10^{-4}$	$4.56 \cdot 10^{-6}$	-2.28	$1.08 \cdot 10^{-5}$
$\zeta_{\text{i,j}}$	0	$-5.12 \cdot 10^{-9}$	$-2.80 \cdot 10^{-9}$	$2.08 \cdot 10^{-10}$	4.18	$-1.01 \cdot 10^{-5}$	8.87
$\beta_{\text{i,j}}$	0.046	-0.011	-0.014	-0.004	$-1.11 \cdot 10^{-5}$	0.011	$1.05 \cdot 10^{-5}$
$\mu_{\text{i,j}}$	0.40	-0.24	-0.05	0.009	$-1.49 \cdot 10^{-4}$	0.033	$1.37 \cdot 10^{-4}$
$\xi_{\text{i,j}}$	$3.1 \cdot 10^{-5}$	$-7.48 \cdot 10^{-4}$	0	0	1.66	0	0
$\chi_{\text{i,j}}$	-1.57	$2.48 \cdot 10^{-5}$	$-4.54 \cdot 10^{-4}$	0	0.95	$-3.83 \cdot 10^{-5}$	0
i,j	1, 1	2, 1	1, 2				
$\gamma_{\text{i,j}}$	$-8.43 \cdot 10^{-7}$	$4.63 \cdot 10^{-8}$	0.36				
$\zeta_{\text{i,j}}$	-0.89	0.070	$2.57 \cdot 10^{-6}$				
$\beta_{\text{i,j}}$	$-1.01 \cdot 10^{-5}$	$1.80 \cdot 10^{-5}$	$6.84 \cdot 10^{-4}$				
$\mu_{\text{i,j}}$	$-1.35 \cdot 10^{-4}$	$2.43 \cdot 10^{-4}$	$6.92 \cdot 10^{-4}$				
$\xi_{\text{i,j}}$	0	0	0				
$\chi_{\text{i,j}}$	-0.32	0	0				

Tab. 3: Hydrostatic restoring coefficients obtained from polynomial interpolation performed without small coefficients

i,j	1, 0	2, 0	3, 0	0, 1	0, 2	0, 3	1, 1	2, 1	1, 2
$\gamma_{i,j}$ (SI)	0.21	−0.12	$2.27 \cdot 10^{-4}$	0	−2.28	0	0	0	0.36
$\zeta_{i,j}$ (SI)	0	0	0	4.22	0	8.95	−0.9	0.07	0

Tab. 4: Wave excitation coefficients obtained from polynomial interpolation performed without small coefficients

i,j	0, 0	1, 0	2, 0	3, 0	0, 2	1, 2
$\beta_{i,j}$ (SI)	0.047	−0.011	−0.014	0.039	0.011	$6.94 \cdot 10^{-4}$
$\mu_{i,j}$ (SI)	0.40	−0.24	−0.05	0.009	0.036	$6.92 \cdot 10^{-4}$
i,j	0, 0	0, 1	1, 1			
$\xi_{i,j}$ (SI)	$3.15 \cdot 10^{-5}$	1.66	0			
$\chi_{i,j}$ (SI)	−1.57	0.95	−0.32			

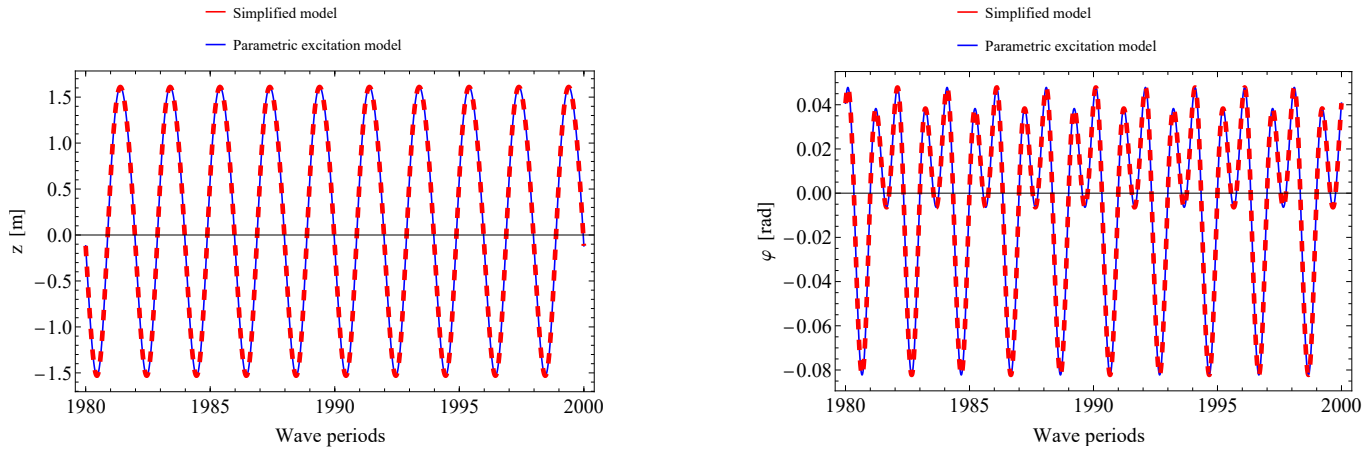

(a) Time series for the heave z

(b) Time series for the pitch φ

Fig. 6: Time series of the solutions of the simplified model (Eqs. (27) and (28)) and the parametric excitation model (Eqs. (2) and (3)) at the steady-state region ($\omega = 1.9$ rad/s, $H = 2.5$ m).

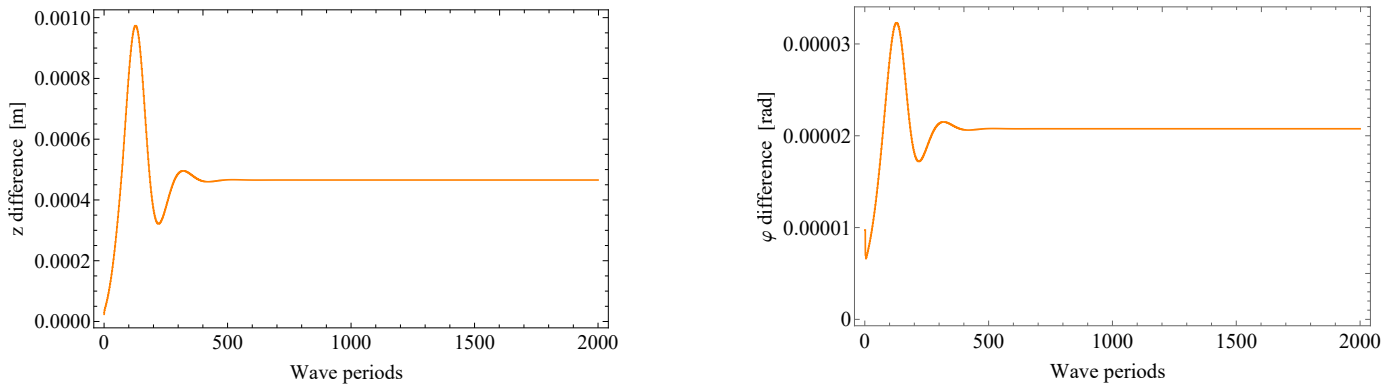

(a) Absolute difference for the heave z

(b) Absolute difference for the pitch φ

Fig. 7: Absolute difference between the solutions of the simplified model (Eqs. (27) and (28)) and the parametric excitation model (Eqs. (2) and (3))

and a backward sweep frequency responses are shown for the test case. In the backward sweep, the oscillation amplitudes indeed kept increasing after parametric resonance was triggered. An estimation of the rms of the unstable branch of the solutions of Eqs. (27) and (28), and a nonlinear fit of the form (the amplitude is expected to exhibit a square-root-type dependency)

$$f(x) = a + \sqrt{|b - cx|}, \tag{33}$$

for the rms are also shown in Fig. 8.

Fig. 9 shows the color map obtained by performing multiple backward sweeps for H varying between 2 m and 3 m.

In Fig. 10, a forward and a backward sweep frequency responses are shown for the test case by using an NLFK force model Giorgi et al. (2021). In this model, both the Froude-Krylov and the hydrostatic restoring forces are calculated using the toolbox developed by Giorgi et al. in Giorgi et al. (2021). The equations for the NLFK force model, are solved in Matlab R2021a. The NLFK force model required computational time more than 10000 times the amount needed for the simplified model (taking a minimum of three hours for a single simulation, while the simulation of the simplified model is less than a second). The reason for such a stark

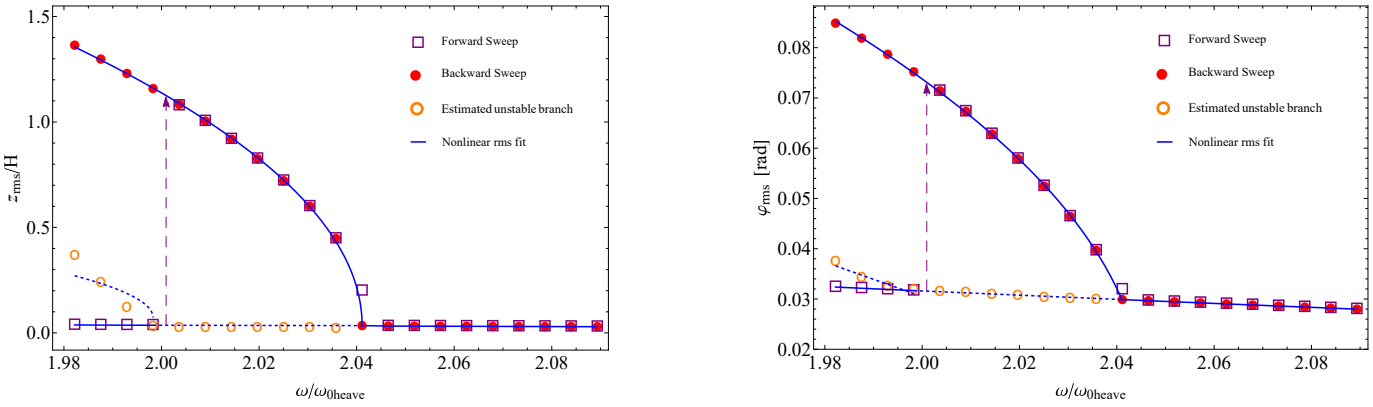

(a) Heave z (b) Pitch φ

Fig. 8: Nonlinear rms fit from the forward and backward sweeps and estimation of the unstable branch of the simplified model, with $H = 2.5$ m, the arrow indicates the amplitude jump due to the loss of stability of the small amplitude steady-state solution

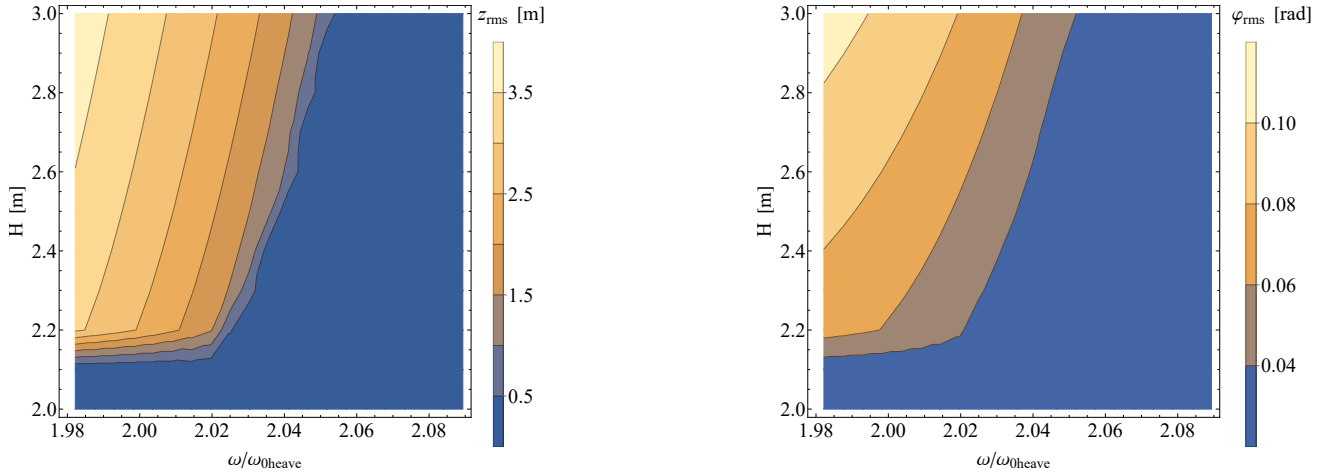

(a) rms for the heave z (b) rms for the pitch φ

Fig. 9: Color map for the backward sweep for the simplified model

difference, is because even though both models are based on the same physical principles, the NLFK force model has to perform a numerical integration to obtain the hydrostatic and the excitation forces multiple times while it solves the equation. The simplified model, on the other hand, uses the much faster offline polynomial interpolations (Eqs (8), (9), (15), and (16)) to calculate the forces. To obtain the coefficients used for simulations in this Section, it took NEMOH approximately 80 minutes. Even considering it, the simplified model is still significantly faster, as these coefficients only have to be calculated once. An estimation of the rms of the unstable branch of the solutions of the model is also shown in Fig. 10. The nonlinear rms fit based on the results are also shown.

The behavior of the amplitudes of the oscillations in both the backward and the forward sweep was similar to the behavior in the simplified model, with 10000-fold speed increase.

6 Conclusion

In this study, we examied a previously presented model for a floating body that captures parametric resonance while being computationally efficient. By nondimensionalizing the system of equations, we determined the significance of the parameters of the model. Some interpolation terms proved to be negligible. The simplified model is able to capture the bifurcation behavior of the system correctly, with the results matching well with the NLFK force model but with increased computational efficiency. On top of this increased computational efficiency, the presented model facilitates analytical approaches, such as perturbation analysis or harmonic balance. These approaches have the potential to facilitate the development of optimization frameworks for spar-buoy design.

One important consideration for further studies is that the models presented in this article, calculate the radiation forces as linearly proportional to the body velocity, with the radiation force coefficient derived considering that the body oscillates at the same frequency as the waves. This is a common approach used for single-frequency waves, which is a simplification of the more general convolution integral required in multi-frequency wave spectra Cummins (1962); Ahmed et al. (2024). However, in the regions where the parametric resonance occurs, the body oscillates at half of the wave frequency. Thus, the applied radiation coefficient considers the wrong oscillation frequency. This will be taken into account in an extension of the model to work with polychromatic waves, as the complete convolution integral for the radiation forces must be used for that case.

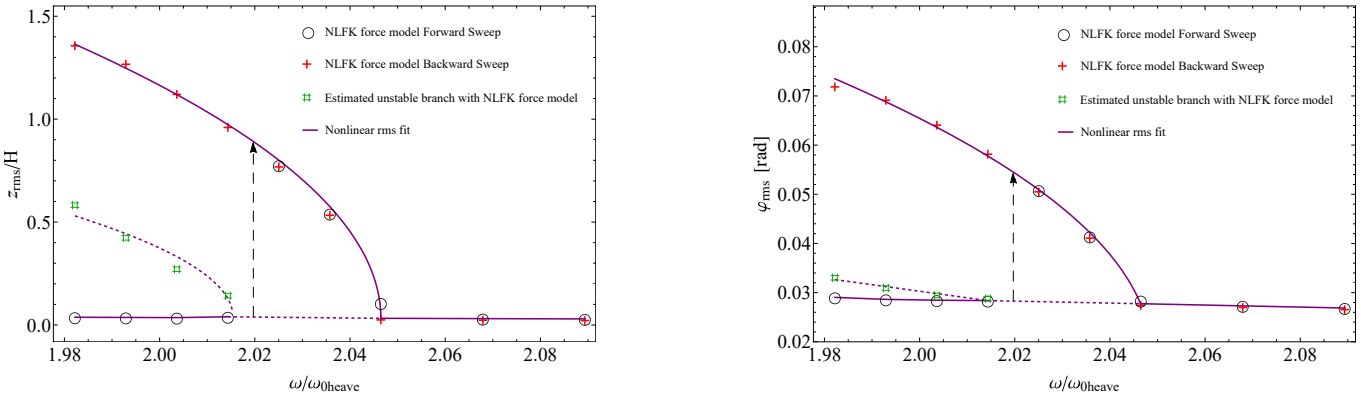

(a) rms for the heave z

(b) rms for the pitch φ

Fig. 10: Nonlinear rms fit and results from the NLFK force model, with $H = 2.5$ m, the arrow indicates the amplitude jump due to the loss of stability of the small amplitude steady-state solution

Acknowledgements

The research reported in this paper is part of project no. TKP-6-6/PALY-2021. Project no. TKP-6-6/PALY-2021 has been implemented with the support provided by the Ministry of Culture and Innovation of Hungary from the National Research, Development and Innovation Fund, financed under the TKP2021-NVA funding scheme. This work has been supported by the Hungarian National Research, Development and Innovation Fund under contracts NKFI K 137726 and K 137699. Erik Silva Fujiyama is funded by the Tempus Public Foundation through the Stipendium Hungaricum Programme. Josh Davidson is funded by MCIN and by the European Union NextGenerationEU/PRTR-C17.I1, as well as by IKUR Strategy under the collaboration agreement between Ikerbasque Foundation and BCAM on behalf of the Department of Education of the Basque Government.

Data availability

The datasets generated during and/or analyzed during the current study are available from the corresponding author on reasonable request.

References

Alaa Ahmed, Lisheng Yang, Jianuo Huang, Ahmed Shalaby, Raju Datla, Lei Zuo, and Muhammad Hajj. Performance characterization and modeling of an oscillating surge wave energy converter. *Nonlinear Dynamics*, 112(6):4007–4025, 2024. doi: 10.1007/s11071-023-09248-2.

Mohsen Azimi. Stability and bifurcation of Mathieu–Duffing equation. *International Journal of Non-Linear Mechanics*, 144: 104049, 2022. doi: 10.1016/j.ijnonlinmec.2022.104049.

Mahdi Aziminia, Abuzar Abazari, Mehdi Behzad, and Masoud Hayatdavoodi. Stability analysis of parametric resonance in spar-buoy based on Floquet theory. *Ocean Engineering*, 266:113090, 2022. ISSN 00298018. doi: 10.1016/j.oceaneng.2022.113090.

Aurélien Babarit and Gérard Delhommeau. Theoretical and numerical aspects of the open source BEM solver NEMOH. In *11th European Wave and Tidal Energy Conference (EWTEC2015)*, Proceedings of the 11th European Wave and Tidal Energy Conference, pages 6–11, Nantes, France, September 2015.

William Edward Cummins. The impulse response function and ship motions. Technical Report, Department of the Navy, David W. Taylor Model Basin, Hydromechanics Laboratory, Research and Development Report, 1962.

Josh Davidson and Tamás Kalmár-Nagy. A real-time detection system for the onset of parametric resonance in wave energy converters. *Journal of Marine Science and Engineering*, 8(10):819, 2020. doi: 10.3390/jmse8100819.

Matt Folley. *Numerical modelling of wave energy converters: state-of-the-art techniques for single devices and arrays*. Academic Press, 2016.

Erik S Fujiyama, Josh Davidson, János Lelkes, and Tamás Kalmár-Nagy. A computationally efficient analytical modelling approach for parametric oscillations in floating bodies. *Journal of Sound and Vibration*, page 119287, 2025. doi: 10.1016/j.jsv.2025.119287.

Elvidio Gavassoni, Paulo B Gonçalves, and Deane M Roehl. Nonlinear vibration modes and instability of a conceptual model of a spar platform. *Nonlinear Dynamics*, 76(1):809–826, 2014. doi: 10.1007/s11071-013-1171-6.

Giuseppe Giorgi, Giovanni Bracco, and Giuliana Mattiazzo. NLFK4ALL: an open-source demonstration toolbox for computationally efficient nonlinear Froude-Krylov force calculations. In *14th WCCM-ECCOMAS Congress*, volume 1500, 2021.

Yong-Pyo Hong, Dong-Yeon Lee, Yong-Ho Choi, Sam-Kwon Hong, and Se-Eun Kim. An experimental study on the extreme motion responses of a spar platform in the heave resonant waves. In *Proceedings of the Fifteenth International Offshore and Polar Engineering Conference. Seoul, Korea*, pages 225–232, 2005.

Hakun Jang and Moohyun Kim. Mathieu instability of arctic spar by nonlinear time-domain simulations. *Ocean Engineering*, 176: 31–45, 2019. doi: 10.1016/j.oceaneng.2019.02.029.

Bonjun Koo, Moohyun Kim, and Robert E Randall. Mathieu instability of a spar platform with mooring and risers. *Ocean Engineering*, 31(17-18):2175–2208, 2004. ISSN 00298018. doi: 10.1016/j.oceaneng.2004.04.005.

Ruddy Kurnia and Guillaume Ducrozet. NEMOH v3.0 user manual. Technical Report, 2022.

Ruddy Kurnia and Guillaume Ducrozet. NEMOH: Open-source boundary element solver for computation of first- and second-order hydrodynamic loads in the frequency domain. *Computer Physics Communications*, 292:108885, 2023. ISSN 00104655. doi: 10.1016/j.cpc.2023.108885.

János Lelkes, Josh Davidson, and Tamás Kalmár-Nagy. Modelling of parametric resonance for heaving buoys with position-varying waterplane area. *Journal of Marine Science and Engineering*, 9(11):1162, 2021. doi: 10.3390/jmse9111162.

Felipe Machado, Norberto Malpica, and Susana Borromeo. Parametric CAD modeling for open source scientific hardware: Comparing Openscad and Freecad Python scripts. *PLOS ONE*, 14(12):e0225795, 2019. doi: 10.1371/journal.pone.0225795.

Ali H Nayfeh and Dean T Mook. *Nonlinear oscillations*. John Wiley & Sons, 2008.

Claudio A Rodríguez and Marcelo AS Neves. Nonlinear instabilities of spar platforms in waves. volume 44915, pages 605–614. American Society of Mechanical Engineers, 2012. doi: 10.1115/OMAE2012-83577.